



Insight into the effect of morphology on catalytic performance of porous CeO₂ nanocrystals for H₂S selective oxidation

Xiaohai Zheng^a, Yanli Li^b, Linyan Zhang^a, Lijuan Shen^{a,*}, Yihong Xiao^a, Yongfan Zhang^b, Chaktong Au^a, Lilong Jiang^{a,*}

^a National Engineering Research Center of Chemical Fertilizer Catalyst, Fuzhou University, Fuzhou, Fujian, 350002, PR China

^b College of Chemistry, Fuzhou University, Fuzhou, Fujian, 350116, PR China



ARTICLE INFO

Keywords:
CeO₂ catalyst
Oxygen vacancy
Crystal facet
DFT calculation
H₂S selective oxidation

ABSTRACT

Shape-specific CeO₂ nanocrystals (rods, cubes, spheres and nanoparticles) with well-defined crystal facets and hierarchically porous structure were successfully synthesized and used as model catalysts to study the structure-dependent behavior and reaction mechanism for H₂S selective oxidation over ceria-based catalysts. It is deduced that the defect sites and base properties of CeO₂ are intrinsically determined by the surface crystal facets. Among the nanocrystals, CeO₂ nanorods with well-defined {110} and {100} crystal facets exhibits superb catalytic activity and sulfur selectivity. The high reactivity for H₂S selective oxidation is attributed to the high concentration of surface oxygen vacancies which are beneficial for the conversion of lattice oxygen to active oxygen species. Besides, the presence of hierarchically porous structure of CeO₂ nanorods hinders the formation of SO₂ and sulfate, ensuring good sulfur selectivity and catalyst stability. Through a combined approach of density-functional theory (DFT) calculations and *in situ* DRIFTS investigation, the plausible reaction mechanism and nature of active sites for H₂S selective oxidation over CeO₂ catalysts have been revealed.

1. Introduction

Hydrogen sulfide (H₂S) is generated in a diversity of chemical processes such as oil refining, natural gas refinery and coal chemistry. Because it is extremely toxic and corrosive, its proper removal is of significance [1,2]. The Claus process is by far the most widely used for desulfurization, recovering elemental sulfur (S) from gaseous hydrogen sulfide. However, limited by thermodynamic limitations, nearly 3–5% H₂S still remains in the tail gas [3], and advanced desulfurization strategies were proposed to circumvent the problem. The photocatalytic splitting of H₂S [4,5] using solar energy is attractive, but the blocking of light and active sites by generated S is a major shortcoming [6]. Among the other desulfurizing processes, that based on catalytic oxidation (H₂S + (1/2)O₂ → (1/n)S_n + H₂O) appears to be promising because H₂S could be effectively and completely converted to elemental sulfur [7]. Numerous metal-oxide catalysts were tested but the results were far from perfect. For example, the use of high-toxicity V₂O₅ is not desirable [8]. As for Fe₂O₃ [9] and TiO₂ [10], catalytic activity or selectivity are unsatisfactory.

With excellent oxygen storage capacity (OSC), superior redox property and versatile acid-base catalytic chemistry, ceria (CeO₂) has

been extensively studied in the field of pollution control [11–14]. CeO₂ has also been considered for the catalytic selective oxidation of H₂S to sulfur [15]. Palma et al. [16] investigated the catalytic properties of V₂O₅-CeO₂ catalysts prepared by impregnation method, which showed high H₂S conversion and sulfur selectivity at low H₂S concentration (500 ppm). Yasyerli et al. [17] reported that owing to Ce⁴⁺/Ce³⁺ redox cycle, there was effective H₂S conversion and high sulfur selectivity over Ce-V mixed oxide. However, with sulfate formation there was fast decline of catalytic activities. The unsatisfactory catalytic activity and instability of the catalysts severely impedes their practical application. It is noted that exploration on the reaction mechanism and nature of active sites of H₂S selective catalytic oxidation is sparse.

Shape control is regarded as a knob for manoeuvring the catalytic properties of metal oxides [18,19]. This is especially true for CeO₂ materials, in which defect sites are highly relevant to the shape of CeO₂ crystals. With well-defined crystal planes, CeO₂ nanocrystals display discrepancy in catalytic performance due to difference in surface energy, atom arrangement and synergistic interaction [20]. In addition, with variation in coordinative unsaturation, Ce⁴⁺ and O²⁻ of CeO₂ facets are different in acid-base property. It is envisaged that the synergism of defect sites and acid-base properties enhances the shape

* Corresponding authors.

E-mail addresses: syhgslj@fzu.edu.cn (L. Shen), jll@fzu.edu.cn (L. Jiang).

dependence of catalytic activity over CeO₂-based catalysts [21]. Despite the many reports on shape dependence of CeO₂ in terms of catalytic performance, the application of CeO₂ in selective oxidation of H₂S is rare and the principle for the design of CeO₂-based catalysts for such an end has not been explored.

On the other hand, the deactivation of CeO₂ is mainly caused by the formation of sulfate and the condensation of produced sulfur inside the catalysts. It was noted that in hierarchical structures, there is the integration of at least two levels of porosity, and with length variation there is the installation of functionality that are favorable for H₂S selective oxidation [22,23]. Therefore, to fully utilize the potential of CeO₂ in H₂S selective oxidation, porosity engineering can serve as an effective strategy to enrich active sites as well as to provide a continuous pathway for mass transport, for example, through the establishment of a stable interconnected open structure [24].

In this work, porous CeO₂ of different shapes were facilely synthesized by hydrothermal methods, and tested in H₂S selective oxidation. Specially, using CeO₂ nanocrystals endowed with well-defined facets as a platform, it is possible to decode their functionalities in catalytic reactions. We elaborately investigated the effect of oxygen vacancies, surface basicity and porous structure on the catalytic activities of ceria in the reaction. We employed density-functional theory (DFT) calculations and in-situ DRIFTS technique to gain insight into the catalytic mechanism and the nature of active sites. To the best of our knowledge, this is the first attempt to systematically study the effect of CeO₂ shapes from the viewpoint of crystal facets. It is expected that the findings could provide guidelines for the optimization of catalyst efficiency in the selective oxidation of H₂S.

2. Experimental

2.1. Preparation of catalysts

All chemical agents in this research were analytical grade and utilized without any purification. CeO₂ with different morphologies were synthesized by a modified hydrothermal method [25]. To obtain CeO₂ nanorods, Ce(NO₃)₃·6H₂O (1.3 g) and urea (4 g) were dissolved in 50 mL of distilled water. Then, 6 mL of NH₃·H₂O was slowly added with stirring into the solution in a stretch of 25 min. Subsequently, the mixture was transferred into a 100 mL Teflon-lined autoclave and heated for 24 h at 150 °C. After the hydrothermal process, the precipitates were separated by centrifugation and washed with ultrapure water and ethanol for three times, then dried at 90 °C overnight, followed by calcination at 500 °C in air for 4 h. The as-prepared nanorods is herein denoted as CeO₂-R. The process for the synthesis of CeO₂ nanospheres (denoted as CeO₂-S) was similar to that for CeO₂-R but with the addition of 10 mmol of polyvinyl pyrrolidone (PVP) and hydrothermal treatment at 180 °C.

To obtain CeO₂ nanocubes (denoted as CeO₂-C), 2.17 g of Ce (NO₃)₃·6H₂O and urea (4 g) were added into 5 mL of distilled water. Meanwhile 9.8 g of NaOH was dissolved in 35 mL of distilled water. The two solutions were mixed with vigorous stirring for about 25 min and transferred to Teflon-lined autoclave (100 mL) keeping the temperature at 100 °C for 24 h. Then the precipitates were separated by centrifugation and washed with ultrapure water and ethanol for three times, followed by drying at 90 °C overnight and calcination at 500 °C for 4 h. The CeO₂ nanoparticles (denoted as CeO₂-N) was prepared by directly adding the same amounts of Ce(NO₃)₃·6H₂O, urea and NaOH into 40 mL of distilled water, and the temperature for hydrothermal treatment was 120 °C.

2.2. Characterization

X-ray diffraction (XRD) data were recorded over an X'Pert3 Powder diffractometer using Cu K α radiation (45 kV, 40 mA). The morphology and structure of samples were studied using a scanning electron

microscope (SEM, Hitachi S-4800), which was also equipped for energy dispersive X-ray (EDX) analysis. N₂ adsorption and desorption isotherms were collected via an U.S. Micromeritics 3Flex analyzer. Raman spectra of catalysts were obtained on a Renishaw spectrometer at ambient condition, and a laser beam ($\lambda = 532$ nm) was used for excitation. Electron paramagnetic resonance (EPR) analysis was carried out using a Bruker E-500 spectrometer operating at 100 kHz. The EPR spectra for all catalysts were recorded at room temperature. Transmission electron microscopy (TEM) and high-resolution transmission electron microscopy (HRTEM) images combined with fast Fourier transform (FFT) analysis were collected on an FEI Tecnai G2 F20 transmission microscope at 200 kV. X-ray photoelectron spectroscopic (XPS) measurements were acquired at 25 °C using a Thermo Scientific ESCALAB 250 spectrometer. The binding energies (BE) were calibrated against the C 1 s X-rays (BE = 284.8 eV) of adventitious carbon.

H₂ temperature-programmed reduction (H₂-TPR), temperature-programmed desorption-mass spectrometry of O₂ (O₂-TPD-MS) and CO₂ (CO₂-TPD-MS) were carried out using AutoChem II 2920 (Micromeritics) instrument coupled with a thermal conductivity detector (TCD). In H₂-TPR measurement, ca. 0.1 g of sample was pre-treated under a helium flow (30 mL/min) at 350 °C for 1 h, followed by cooling to room temperature. The TPR profiles were obtained from 50 to 900 °C at a rate of 10 °C/min in a 10% H₂/Ar flow. As for O₂-TPD-MS, after 0.1 g of sample was heated for 1 h at 350 °C under helium and cooled to 25 °C, O₂ (30 mL/min) was steadily directed into the sample tube for 1 h. Then O₂ desorption was carried out in a helium flow (30 mL min⁻¹) from 50 to 900 °C. As for CO₂-TPD-MS analysis, pre-treatment was similarly conducted, and pure CO₂ gas was continually pulsed in for 1 h. CO₂ desorption was monitored in the temperature range of 50–900 °C.

in situ diffuse reflection infrared Fourier transform spectroscopy (*in situ*-DRIFTS) of H₂S adsorption over the CeO₂ catalysts was collected by a Nicolet-6700 FTIR spectrometer at 2 cm⁻¹ resolution (64 scans). Prior to each experiment, the catalyst was heated in a helium flow at 300 °C for 1 h (for the removal of surface impurities), then cooled to 100 °C for the collection of background spectrum. Afterward, 5000 ppm of H₂S in helium was introduced to the cell at 100 °C and DRIFTS spectrum was recorded. The above process was iterated and DRIFTS spectrum was collected at designated temperatures (130, 160, 190, 220 and 250 °C).

2.3. Catalytic performance evaluation

H₂S selective oxidation reactions were performed in a conventional fixed-bed steel reactor with TCD and flame photometric detector (FPD) at atmospheric pressure as illustrated in Fig. S1. The catalyst (0.2 g of 20–40 mesh) was placed in the central section of reactor. The feed (35 mL/min) which contained 5000 ppm H₂S, 2500 ppm O₂ and helium was introduced into the reactor at a weight hourly space velocity (WHSV) of 10 500 mL g⁻¹ h⁻¹ at designated temperatures in the range of 100–250 °C. A condenser next to the reaction tube was used to trap sulfur in the off-gas. The H₂S conversion (X_{H2S}), sulfur yield, and sulfur selectivity (S_{sulfur}) were defined according to the following equations:

$$X_{H_2S} = \frac{[H_2S]_{in} - [H_2S]_{out}}{[H_2S]_{in}}$$

$$S_{sulfur} = \frac{[H_2S]_{in} - [H_2S]_{out} - [SO_2]_{out}}{[H_2S]_{in} - [H_2S]_{out}}$$

$$\text{Sulfur yield} = [X_{H2S}] \times [S_{sulfur}]$$

For the reactions conducted at large WHSV (48 000 mL g⁻¹ h⁻¹) for the elimination of external and internal diffusion, the turnover frequencies TOF (s⁻¹) and reaction rate r_{H2S} (mol·g⁻¹·s⁻¹) were calculated using the following formulas:

$$\text{TOF}_{\text{H}_2\text{S}} = \frac{X_{\text{H}_2\text{S}} \times C_0 \times V_{\text{gas}}}{n} (\text{s}^{-1})$$

$$r_{\text{H}_2\text{S}} = \frac{X_{\text{H}_2\text{S}} \times C_0 \times V_{\text{gas}}}{m} (\text{mol}\cdot\text{g}^{-1}\cdot\text{s}^{-1})$$

Here, $X_{\text{H}_2\text{S}}$ stands for the H_2S conversion at 220 °C, C_0 (mol/s) is the initial H_2S concentration in the inlet gas and V_{gas} is the total molar flow rate. As for n and m , they represent the molar mass and mass of catalyst, respectively.

2.4. DFT calculations

2.4.1. Computation method

Density functional theory (DFT) plane-wave calculations were conducted utilizing the Vienna ab initio simulation package VASP [26,27] with the Projector Augmented Wave (PAW) method. We used the generalized gradient approximation (GGA) with the Perdew-Burke-Ernzerhof (PBE) [28] exchange-correlation functional, and a kinetic cut-off energy of 450 eV was used. We adopted the PBE plus on-site repulsion U (PBE + U) method to correct the strong on-site Coulomb interaction of strong localized Ce 4f electrons, and the U_{eff} parameter of 4.5 eV was used for Ce atoms [29]. All the calculations were performed by utilizing the Brillouin zone respectively sampled with $(1 \times 1 \times 1)$ and $(3 \times 3 \times 3)$ k-point grids Monkhorst-Pack mesh for the surface and bulk. Atomic positions were optimized until a force of below 0.03 eV/Å was reached, and spin polarizations were performed in all calculations.

2.4.2. Surface model

In a unit cell of CeO_2 , fourfold-coordinated O ions provide a cubic close-packed layer and cerium ions are distributed in the half of eightfold-coordinated cationic sites (Fig. S2A, Supporting Information). For surface models, stoichiometric CeO_2 {110} was simulated by a supercell slab of $10.929 \text{ \AA} \times 11.592 \text{ \AA}$ having six atomic layers. The CeO_2 {100} and {111} surfaces were constructed in a supercell by a slab of $11.592 \text{ \AA} \times 11.592 \text{ \AA}$ and $15.456 \text{ \AA} \times 11.592 \text{ \AA}$ of nine atomic layers (Fig. S2), respectively. The spacing between adjacent slabs was set as 12 \AA and the reduced CeO_2 surface was constructed by the removal of an O atom from the top layer.

The adsorption energy (E_{ad}) is used to measure the intensity of adsorbate-substrate interaction, which was calculated by $E_{\text{ad}} = E[\text{CeO}_{2-x} + \text{adsorbate}] - E[\text{CeO}_{2-x}] - E[\text{adsorbate}]$, in which $E[\text{CeO}_{2-x} + \text{adsorbate}]$ is the total electronic energy of reduced CeO_2 surface with adsorbate entity, $E[\text{CeO}_{2-x}]$ and $E[\text{adsorbate}]$ are the energies of reduced CeO_2 surface and a free molecule, respectively. The energy (E_{dis}) for H_2S and SH dissociation on the ceria {110} surface are defined as: $E_{\text{dis}} = E_{\text{after}} - E_{\text{before}}$, where E_{before} and E_{after} stand for the total energy before and after dissociation, respectively. The adsorption and dissociation energies were calculated according to the energy difference between the initial and final states of optimized structures in the reaction. According to these definitions, larger negative value indicates stronger exothermic interaction between surface and adsorbate.

3. Results and discussions

3.1. Morphological characteristics and structural properties

As revealed in the SEM images displayed in Fig. 1, the targeted ceria samples were successfully fabricated via the adopted hydrothermal methods. It can be seen that $\text{CeO}_2\text{-R}$ is made up of rods $\sim 20 \text{ nm}$ in diameter and $100\text{--}300 \text{ nm}$ in length (Fig. 1A). Fig. 1B shows that $\text{CeO}_2\text{-C}$ is composed of cubes with smooth surface and with size varying from 30 to 50 nm . As for $\text{CeO}_2\text{-S}$ (Fig. 1C), it is made up of spheres with rough surfaces, and the average diameter is $\sim 300 \text{ nm}$. As shown in Fig. 1D, the $\text{CeO}_2\text{-N}$ sample displays random nanoparticles that are $10\text{--}50 \text{ nm}$ in size.

Ceria with shape specificity usually exposes distinct surfaces,

making experimental investigations on the relationship between catalytic performance and specific morphology possible. The TEM image of Fig. 2A confirms the rod-like morphology of $\text{CeO}_2\text{-R}$. The HRTEM image combined with FFT pattern (inset) in Fig. 2B reveal that the surface of $\text{CeO}_2\text{-R}$ is dominated by {220} and {200} crystal faces showing interplanar spacing of 0.19 and 0.27 nm , which belong to {110} and {100} facets, respectively [30,31]. In addition, the inset image in Fig. 2A shows that $\text{CeO}_2\text{-R}$ possesses a porous structure that extends throughout the nanorods. The average size of the uniform mesopores is about 10 nm , and the generation of porous structure might be attributed to the release of gaseous products during the synthetic procedure as a result of urea thermal decomposition $(\text{CO}(\text{NH}_2)_2 + 2\text{H}_2\text{O} \rightarrow 2\text{NH}_3 + \text{CO}_2)$. It can be observed from Fig. 2(C, D) that $\text{CeO}_2\text{-C}$ is with {200} facets having interplanar spacing of 0.27 nm . The spheres of $\text{CeO}_2\text{-S}$ (Fig. 2E) is enclosed by {200} and {111} facets with interplanar spacing of 0.27 and 0.31 nm , respectively (Fig. 2F). There are voids detected in the morphology of $\text{CeO}_2\text{-S}$, suggesting that the spheres are made up of loosely agglomerated ceria nanoparticles. As seen from Fig. 2(G, H), the surface of $\text{CeO}_2\text{-N}$ is dominated by {111} crystal face with interplanar spacing of 0.31 nm , which are thermodynamically the most stable among crystal facets [32,33]. In summary, $\text{CeO}_2\text{-C}$ exhibits {100} while $\text{CeO}_2\text{-N}$ {111} facets. As for $\text{CeO}_2\text{-R}$ and $\text{CeO}_2\text{-S}$, the former has {100} and {110} while the latter {100} and {111} facets. With variation in terms of exposed facets, the ceria samples should be different in chemical property, and hence exhibit distinct catalytic performance for H_2S selective oxidation.

The phase structures of $\text{CeO}_2\text{-R}$, $\text{CeO}_2\text{-C}$, $\text{CeO}_2\text{-S}$ and $\text{CeO}_2\text{-N}$ were investigated by XRD (Fig. 3A). The characteristic diffraction peaks at $2\theta = 28.7, 33.2, 47.4, 56.4, 59.2, 69.3, 76.5$, and 79.1° are attributable to {111}, {200}, {220}, {311}, {222}, {400}, {331}, and {420} planes of face-centered cubic (fcc) fluorite structure (space group: $\text{O}_h^5\text{-Fm}3m$) of CeO_2 crystals (JCPDS 34-0394) [34]. Note that the diffraction peaks of the four CeO_2 catalysts are different in intensity and full width at half maximum (FWHM), suggesting variation in crystallite size and crystallinity. The lattice parameters, crystallite sizes and crystallinity calculated from the XRD peaks are summarized in Table 1. It is clearly found that the four samples are similar in lattice parameter.

It is well acknowledged that the major defect of CeO_2 catalysts is oxygen vacancies, which often acts as active sites on metal oxides for catalytic reactions [35–37]. Moreover, the generation of oxygen vacancies on CeO_2 materials is highly surface sensitive. According to the results of Raman analysis (Fig. 3B), all catalysts show a strong peak at around 458 cm^{-1} attributable to the F_{2g} vibrational mode of ceria with fluorite-type structure that can be viewed as symmetric breathing of oxygen anions around cerium cations [38]. There are three additional bands at $255, 598$ and 1172 cm^{-1} , attributed to modes of second-order transverse acoustic (2TA), defect-induced (D) ($\text{O}_0^x + 2\text{Ce}_0^x \rightarrow \text{V}_0^{\bullet} + 2\text{Ce}_0^{\bullet} + \frac{1}{2}\text{O}_2$), and longitudinal optical (2LO), respectively. The difference in wavenumber between the defect and F_{2g} bands is $\sim 140 \text{ cm}^{-1}$, suggesting that oxygen vacancies of CeO_2 catalyst are generated from intrinsic defects ($\text{Ce}^{4+} \rightarrow \text{Ce}^{3+}$) [39]. In Raman investigation of CeO_2 catalysts, the $I_{(598+1172)/I_{458}}$ intensity ratios were calculated for quantifying the concentration of intrinsic defects (oxygen vacancies) [40]. It is apparent that the $I_{(598+1172)/I_{458}}$ ratios of catalysts are dependent on CeO_2 morphologies, and increase in the following order: $\text{CeO}_2\text{-N}$ (0.08) $<$ $\text{CeO}_2\text{-S}$ (0.13) $<$ $\text{CeO}_2\text{-C}$ (0.15) $<$ $\text{CeO}_2\text{-R}$ (0.21). Among the four, $\text{CeO}_2\text{-R}$ is the highest in intrinsic defect sites and oxygen vacancies, followed by $\text{CeO}_2\text{-C}$ and $\text{CeO}_2\text{-S}$, while $\text{CeO}_2\text{-N}$ is the lowest. EPR spectroscopy was performed to further verify the presence of oxygen vacancies. As shown in Fig. 3C, the four CeO_2 catalysts show two signals at $g_{\perp} = 1.96$ and $g_{\parallel} = 1.94$, which are ascribed to Ce^{3+} located in the bulk and on the surface of CeO_2 nanocrystals [41], respectively. It is observed that the signal intensity corresponding to the concentration of oxygen vacancies follows the sequence of $\text{CeO}_2\text{-N} < \text{CeO}_2\text{-S} < \text{CeO}_2\text{-C} < \text{CeO}_2\text{-R}$, in accord with the trend obtained in Raman analysis. According to the vacancy-

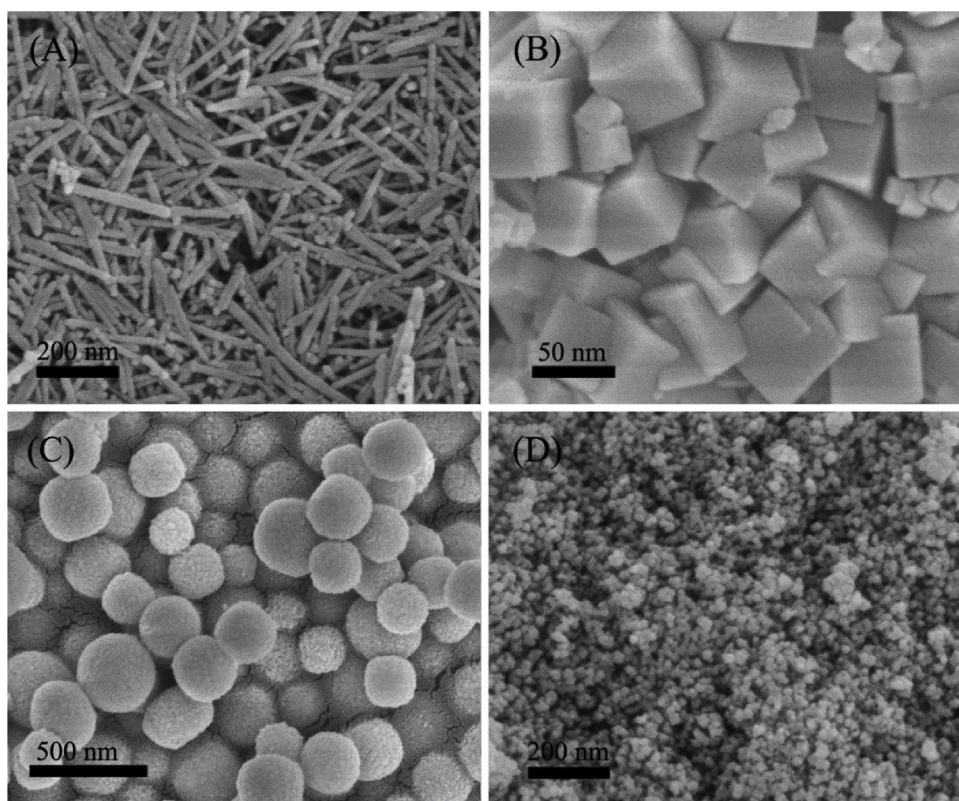


Fig. 1. SEM images of CeO_2 catalysts: (A) $\text{CeO}_2\text{-R}$, (B) $\text{CeO}_2\text{-C}$, (C) $\text{CeO}_2\text{-S}$ and (D) $\text{CeO}_2\text{-N}$.

hopping mechanism, the presence of oxygen vacancies (such as linear surface oxygen vacancies) is favorable for oxygen migration [42]. The enrichment of oxygen vacancies on $\text{CeO}_2\text{-R}$ with $\{110\}$ and $\{100\}$ crystal planes would prompt the diffusion of bulk oxygen to the surface and provide the catalyst with more active oxygen for enhanced reactivity and reducibility.

XPS analysis was conducted to elucidate the chemical states of surface Ce and O species. The Ce 3d spectra of catalysts are shown in Fig. 3D, and they could be resolved into eight groups. The peaks labeled “U” and “V” are $3d_{3/2}$ and $3d_{5/2}$ signals of cerium, displaying spin-orbit splitting of 18.4 eV [43]. The $3d_{3/2}$ peaks labeled U (901.5 eV), U' (907.7 eV) and U'' (917.1 eV) and the $3d_{5/2}$ peaks labeled V (882.4 eV), V'' (889.2 eV) and V''' (898.1 eV) are ascribed to Ce^{4+} . In addition, the U' (903.2 eV) and V' (884.9 eV) components are ascribed to Ce^{3+} species. It is known that the Ce^{3+} proportion could be related to the amount of oxygen vacancies (V_o) on CeO_2 surfaces [44]. Based on the peaks areas of Ce^{3+} and Ce^{4+} signals, calculation on the proportion of surface Ce^{3+} expressed as $\text{Ce}^{3+}/(\text{Ce}^{3+} + \text{Ce}^{4+})$ was performed, and the results are listed in Table S1. It is clearly observed that the $\text{Ce}^{3+}/(\text{Ce}^{3+} + \text{Ce}^{4+})$ ratios increase in the sequence $\text{CeO}_2\text{-N} < \text{CeO}_2\text{-S} < \text{CeO}_2\text{-C} < \text{CeO}_2\text{-R}$, which is in line with that of formation energy for the generation of oxygen vacancies on CeO_2 crystal facets [45]. It is hence deduced that being highest in Ce^{3+} percentage, $\text{CeO}_2\text{-R}$ is the highest in the amount of surface oxygen vacancies among the four catalysts.

The O 1s profiles of the CeO_2 catalysts (Fig. S3) could be deconvoluted into three peaks located at ca. 528.7, 530.2 and 532.8 eV, assignable to lattice oxygen (O_{latt}), chemisorbed oxygen species and weakly bound oxygen species (O_{ad}), respectively [46]. It is accepted that the concentration of oxygen vacancies could be described by the $O_{ad}/(O_{latt} + O_{ad})$ ratio [47], and the related results are shown in Table S1. It is clear that the ranking of $O_{ad}/(O_{latt} + O_{ad})$ ratios follows the order of: $\text{CeO}_2\text{-N} < \text{CeO}_2\text{-S} < \text{CeO}_2\text{-C} < \text{CeO}_2\text{-R}$, which matches well with the order based on the Ce 3d signals. The results demonstrate that

the number of Ce^{3+} sites is proportional to that of surface active oxygen species, and the former have the ability to activate and transfer oxygen. According to the literature [48], a high concentration of oxygen vacancies would enhance the formation of disordered oxygen in the ceria lattice, consequently facilitating the diffusion of oxygen from bulk to surface. Based on the results above, it can be concluded that being distinct in crystallographic facets, CeO_2 of different shapes display variation in concentration of oxygen vacancies, leading to performance discrepancy in H_2S selective oxidation.

The N_2 adsorption isotherms of the catalysts presented in Fig. 4A correspond to type IV curves, which signify mesopores with good pore connectivity [49]. The adsorption branches of isotherms for $\text{CeO}_2\text{-R}$ and $\text{CeO}_2\text{-S}$ resemble that of type II, indicating the presence of macropores. The H3 hysteresis loops of $\text{CeO}_2\text{-R}$ and $\text{CeO}_2\text{-S}$ in the range of $P/P_0 = 0.5\text{--}1.0$ imply the existence of slit-like pores in the catalysts, while $\text{CeO}_2\text{-C}$ and $\text{CeO}_2\text{-N}$ possess H1-type hysteresis loops, suggesting positive mesostructure of cylindrical mesopores [50]. The pore-size distribution curves of CeO_2 nanostructures based on the Barrett-Joyner-Halenda (BJH) method are presented in Fig. 4B. It is obvious that $\text{CeO}_2\text{-R}$ shows a hierarchically multimodal porous structure with double apexes at 13.8 nm and 30.5 nm. The $\text{CeO}_2\text{-C}$ catalyst also exhibits two peaks, one at 8.2 nm and the other at 14.4 nm, which are caused by the open ends and stacking of nanocubes, respectively. In addition, both $\text{CeO}_2\text{-R}$ and $\text{CeO}_2\text{-S}$ exhibit a small amount of macropores, owing to tight stacking of nanorods and nanoparticles in the nanospheres. The presence of bi-modal porous architecture has a positive effect on the enhancement of catalytic activity because the inter-connected internal void space could act as effective transport pathways [51]. Table 1 depicts the pore structure parameters of the four CeO_2 samples. The results show that the specific surface areas and pore volume of the catalysts are in a decreasing order of $\text{CeO}_2\text{-R} > \text{CeO}_2\text{-C} > \text{CeO}_2\text{-S} > \text{CeO}_2\text{-N}$.

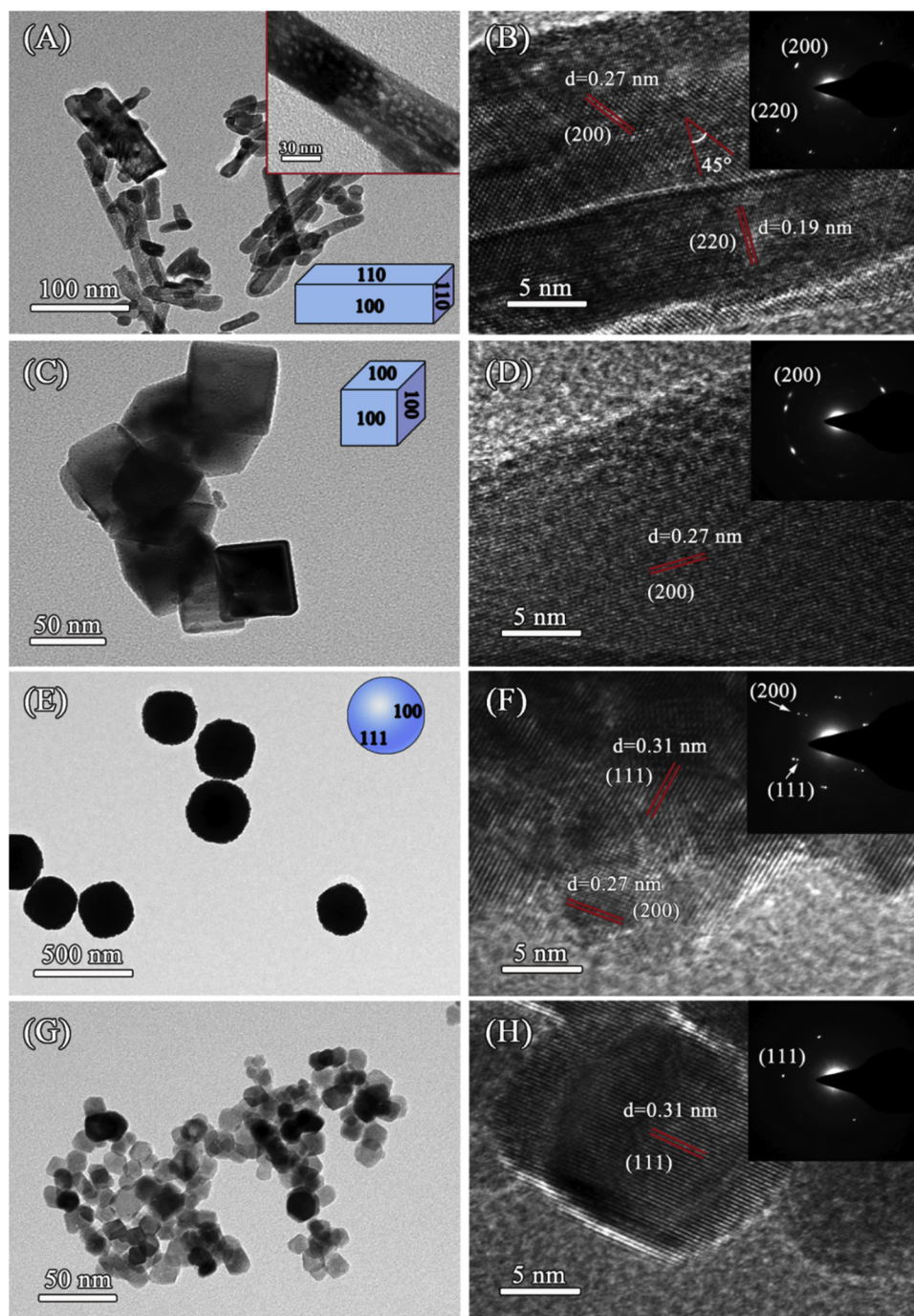


Fig. 2. TEM images (left column), corresponding HRTEM images (right column) and FFT pattern (insets) of CeO_2 catalysts: (A, B) $\text{CeO}_2\text{-R}$, (C, D) $\text{CeO}_2\text{-C}$, (E, F) $\text{CeO}_2\text{-S}$ and (G, H) $\text{CeO}_2\text{-N}$.

3.2. Catalytic performance

The H_2S conversion in the oxidation reaction is greatly dependent on reaction temperature because the activation energy (E_a) for H_2S oxidation ($\sim 40 \text{ kJ/mol}$) is less than that of sulfur oxidation ($125 \pm 10 \text{ kJ/mol}$) [52]. As displayed in Fig. 5A, the H_2S conversions over the four CeO_2 catalysts gradually increase and eventually reach 100% as the temperature increasing from 100 to 250 °C. It is observed that $\text{CeO}_2\text{-R}$ is the most active, followed by $\text{CeO}_2\text{-C}$ and $\text{CeO}_2\text{-S}$ with $\text{CeO}_2\text{-N}$ the least active. Over $\text{CeO}_2\text{-R}$ and $\text{CeO}_2\text{-C}$, H_2S conversion reaches 100% at 220 °C, whereas over $\text{CeO}_2\text{-S}$ and $\text{CeO}_2\text{-N}$ H_2S conversion reaches 100% at 250 °C. The Raman, EPR and XPS analyses shown in Fig. 3 demonstrate that the $\text{CeO}_2\text{-R}$ catalyst endowed with

{110} and {100} crystal planes shows largest amount of oxygen vacancies, which would promote the diffusion of bulk oxygen to the surface and provides the catalyst with more active oxygen for the enhancement of reactivity and reducibility. Therefore, the $\text{CeO}_2\text{-R}$ catalyst exhibits the highest H_2S conversion, higher than those of the Ce-based catalysts compiled in Table S2. The sulfur selectivity over the four catalysts is affected by the shape and crystal plane as presented in Fig. 5B. Over $\text{CeO}_2\text{-R}$, sulfur selectivity remains close to 100% at the temperature range of 100–250 °C. As for $\text{CeO}_2\text{-C}$, sulfur selectivity starts to decrease when the reaction temperature is higher than 200 °C, while that of $\text{CeO}_2\text{-S}$ and $\text{CeO}_2\text{-N}$ starts to decrease at 190 °C plausibly due to side reactions ($\text{H}_2\text{S} + 3/2 \text{ O}_2 \rightarrow \text{SO}_2 + \text{H}_2\text{O}; \text{S} + \text{O}_2 \rightarrow \text{SO}_2$) [53]. Overall, sulfur selectivity of CeO_2 catalysts decreases in the following

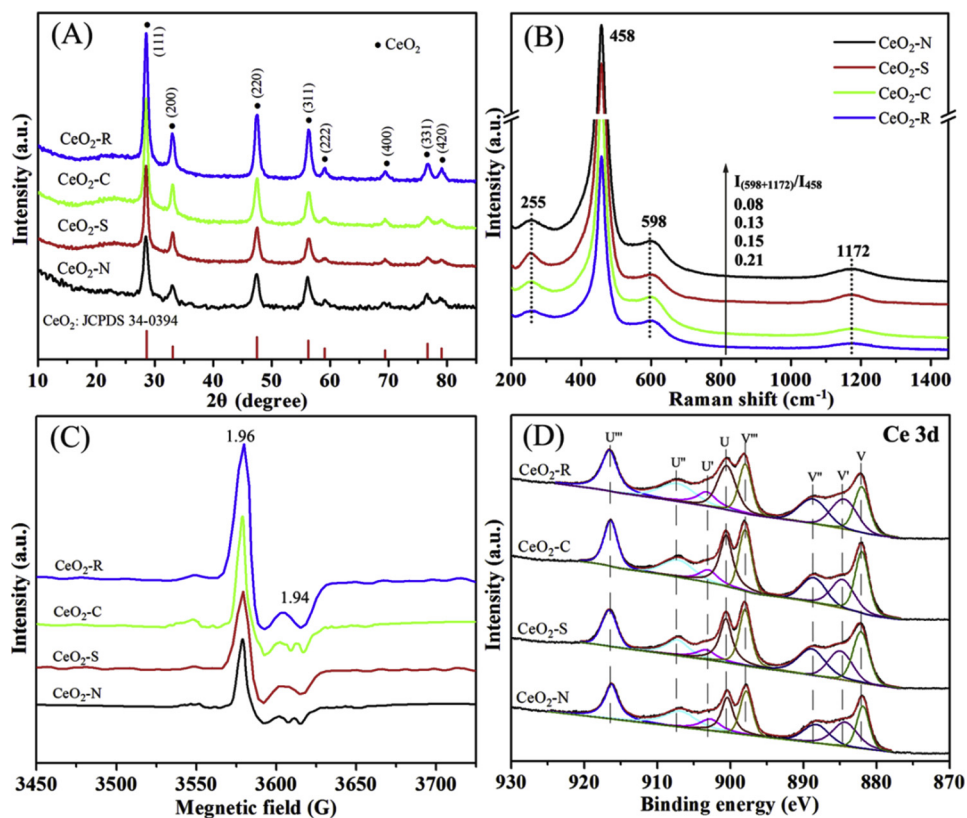


Fig. 3. (A) XRD patterns, (B) Raman spectra, (C) EPR spectra, and (D) Ce 3d XPS spectra of CeO₂-R, CeO₂-C, CeO₂-S and CeO₂-N.

order: CeO₂-R > CeO₂-C > CeO₂-S > CeO₂-N. It is noted that the sulfur selectivity over the four CeO₂ catalysts is higher than 90% in the temperature range adopted for the investigation.

The sulfur yields of the CeO₂ catalysts are depicted in Fig. 5C. Note that when the reaction temperature is below 190 °C, the variance tendency is close to that of H₂S conversion on account of 100% sulfur selectivity. Above 190 °C, the sulfur yield over CeO₂-C starts to decrease due to the decline of sulfur selectivity. Nevertheless, CeO₂-R catalyst achieves highest sulfur yield (100%) at 250 °C, while the sulfur yield of CeO₂-N catalyst is only 90%. The sulfur collected from the effluent (Fig. S4) and that incorporated into the used catalyst were calculated by mass balance, and the total is close to the sulfur yield [54]. Based on the above results, it is deduced that the catalytic activity of ceria catalysts in oxidative desulfurization strongly depends on the shape of ceria nanocrystals. As for the main factors that affect catalytic activity, it will be discussed in detail in the later section.

The kinetic studies of H₂S selective oxidation over the four catalysts were conducted at 100–250 °C having H₂S conversion kept below 20% to eliminate internal and external diffusion limitations [55]. Natural logarithm of H₂S conversion (lnk) versus the reciprocal of reaction temperature was plotted as depicted in Fig. 5D, and the apparent activation energy E_a for the catalysts were calculated. It is found that the E_a values increase in the following order: CeO₂-R > CeO₂-C > CeO₂-

N > CeO₂-S, which is in accord with the results of catalytic activity. Being lowest in activation energy (26.5 kJ/mol), CeO₂-R is the most active among the four CeO₂ catalysts. The results disclose that CeO₂-R with well-defined {100} and {110} planes is the most efficient for selective oxidation of H₂S. In addition, the good linear plots (correlation coefficient: 0.9876 < R² < 0.9918) of all the catalysts indicates that H₂S conversion rate is strongly dependent on reaction temperature [56]. According to the activity results, the reaction rates and TOFs over the CeO₂ catalysts were calculated, and the results are summarized in Table 2. It is observed that the ranking of TOF values and reaction rates follow the order of CeO₂-R > CeO₂-C > CeO₂-S > CeO₂-N, indicating the high availability of active sites on CeO₂ of rod-like morphology [57]. In addition, the results highlight the obvious effect of exposed CeO₂ crystal planes on H₂S selective oxidation. In order to find out the key factor that determines the H₂S conversion over the CeO₂ catalysts, we normalized the intrinsic activity to exclude the effect of specific surface areas on activities (Table S3). The results show that CeO₂-R is the highest in terms of normalized H₂S conversion, indicating that specific surface area could not be the decisive factor for H₂S conversion, whereas the presence of the {100} and {110} facets is responsible for its superb H₂S conversion.

The CeO₂-R catalyst was chosen to investigate the effect of WHSV, H₂S/O₂ molar ratio in feed and water vapor on catalytic performance.

Table 1

Lattice parameters, crystallinity and textural parameters of CeO₂ materials with different shapes.

Samples	Lattice parameter ^a (nm)	Crystal size ^b (nm)	Crystallinity (%)	Surface area (m ² /g)	Pore volume (cm ³ /g)	Average pore size (nm)
CeO ₂ -R	0.5405	19.7	28.7	87.2	0.58	20.5
CeO ₂ -C	0.5409	13.5	23.5	65.5	0.47	10.2
CeO ₂ -S	0.5403	27.3	31.8	62.8	0.43	28.6
CeO ₂ -N	0.5406	16.5	26.4	56.1	0.21	16.7

^a For fluorite phase, calculated by the Bragg equation ($2d \sin\theta = n\lambda$).

^b Based on Scherrer equation using the (111) peaks.

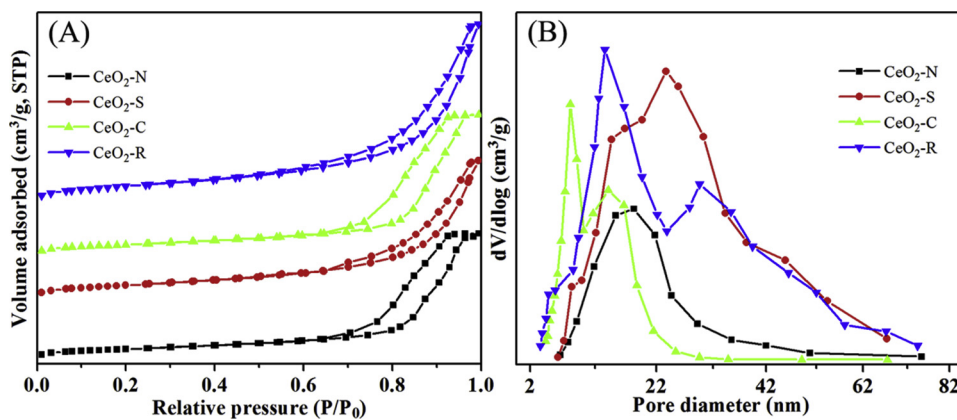


Fig. 4. (A) N₂ adsorption-desorption isotherms and (B) pore diameter distributions of CeO₂ with different shapes.

The effect of H₂S/O₂ molar ratio was investigated at 220 °C. The H₂S concentration was kept constant at 5000 ppm and the H₂S/O₂ molar ratio was varied from 3:1 to 1:2. As illustrated in Fig. 6A, the CeO₂-R catalyst shows 94.5% H₂S conversion and 100% sulfur selectivity at a H₂S/O₂ ratio of 3:1. With the decrease of H₂S/O₂ molar ratio to 2:1, H₂S conversion and sulfur selectivity are close to 100%. Further decrease of H₂S/O₂ molar ratio from 1:1 to 1:2 has no obvious influence on H₂S conversion, but there is decrease of sulfur selectivity from 95% to 85%. In addition, the sulfur yield first increases to 100% when the H₂S/O₂ molar ratio reaches stoichiometric proportion (2:1) and then decreases with increasing O₂ concentration. The results demonstrate that a low O₂ concentration (*i.e.*, insufficient O₂ supply) results in lower H₂S conversion, while a high O₂ concentration (excess O₂) promotes the deep oxidation of H₂S) causes decrease of sulfur selectivity [58,59]. Thus, the H₂S/O₂ molar ratio has governing power on H₂S conversion and sulfur selectivity in the reaction of H₂S selective oxidation.

The influence of WHSV on catalytic performance was performed at 220 °C with WHSV varying from 7500 to 15 000 mL·g⁻¹ h⁻¹. As

illustrated in Fig. 6B, when WHSV is below 10 500 mL·g⁻¹ h⁻¹, H₂S conversion is 100%. With further increase of WHSV, there is gradual decrease of H₂S conversion. It can be noted that sulfur selectivity remains close to 100% in the WHSV range of 7500 to 15 000 mL·g⁻¹ h⁻¹. Despite decrease of H₂S conversion at high WHSV, the sulfur yield over CeO₂-R is still higher than 90% due to the high sulfur selectivity.

The H₂S gas generated in a diversity of industrial processes always contains a certain amount of water, which would cause deactivation of desulfurization catalysts [60]. Therefore the effect of water vapor on H₂S selective oxidation was investigated over CeO₂-R at 220 °C. As presented in Fig. 6C, both H₂S conversion and sulfur selectivity stay close to 100% when water vapour of 5 vol% was introduced to the feed. With further rise of water vapor content, there is gradual decline of H₂S conversion and sulfur yield. The sulfur selectivity starts to decrease when the water vapor content exceeds 15 vol%. As shown in Fig. S5, the adding of 10 vol% water vapour after an on stream time of 5 h results in gradual decline of H₂S conversion from *ca.* 100% to 96%, and such a state remains in the following 17 h, indicating that the presence of H₂O

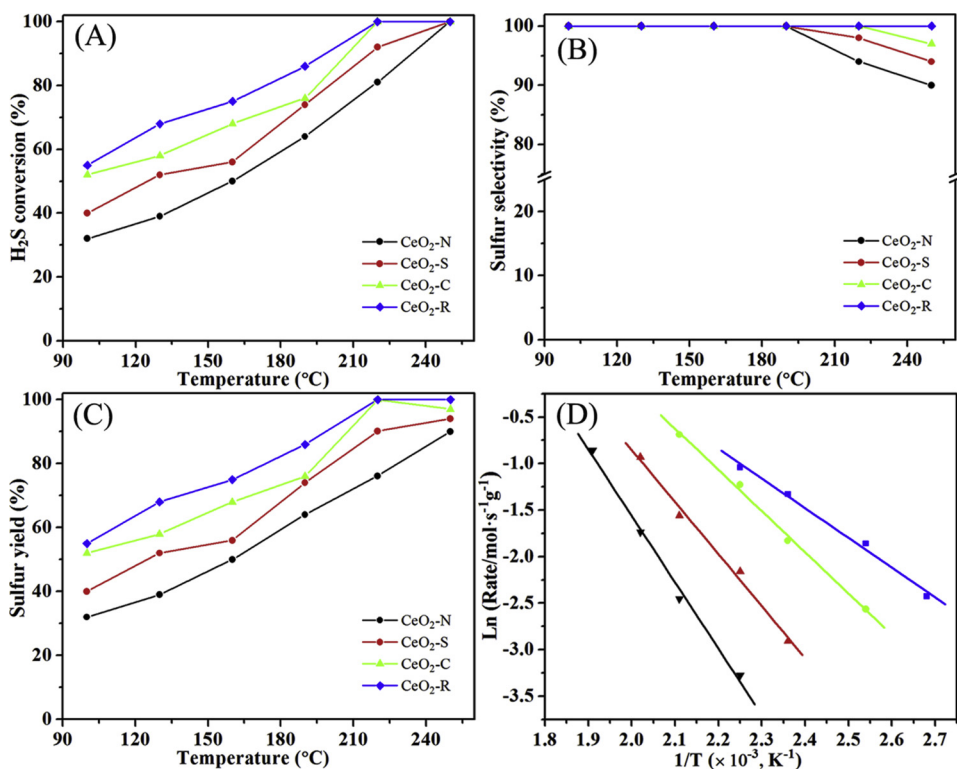
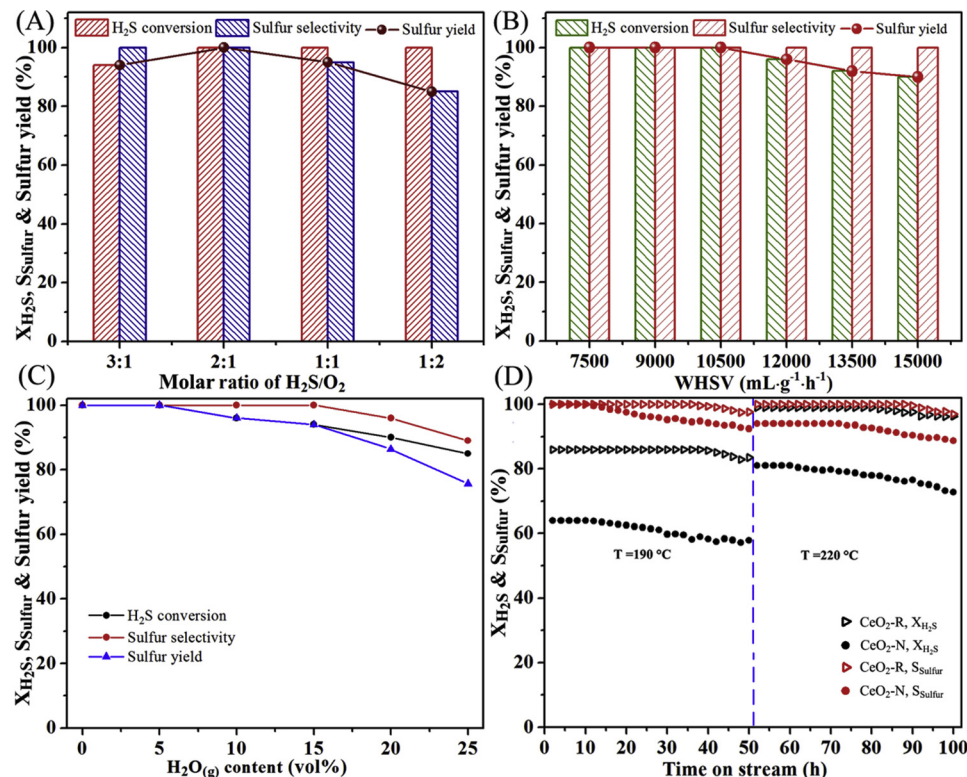


Fig. 5. (A) H₂S conversion, (B) sulfur selectivity, (C) sulfur yield, and (D) Arrhenius plots for H₂S oxidation over the four CeO₂ catalysts.

Table 2Reaction rates, E_a and TOF values for H_2S oxidation over the CeO_2 catalysts.

Catalysts	Exposed facet	Reaction rate ($\times 10^{-7}$ mol·g $^{-1}$ ·s $^{-1}$)	E_a (kJ/mol)	TOF values ($\times 10^{-5}$ s $^{-1}$)
CeO_2 -R	{100} + {110}	2.41	26.5	4.14
CeO_2 -C	{100}	2.12	36.8	3.65
CeO_2 -S	{100} + {111}	1.78	46.4	3.06
CeO_2 -N	{111}	1.33	59.3	2.29

**Fig. 6.** Effect of (A) H_2S/O_2 molar ratio, (B) WHSV, (C) $H_2O(g)$ content on catalytic performance of CeO_2 -R catalyst; (D) Time on stream behavior of the CeO_2 -R and CeO_2 -N catalysts (X_{H_2S} stands for H_2S conversion and S_{Sulfur} for sulfur selectivity).

leads to partial deactivation of catalyst. Upon the removal of water vapor, the H_2S conversion slowly returns to 100%. The slight decrease in catalytic activity upon water vapor containing condition might be owing to competition between water vapor and H_2S at the active sites [61]. The results above demonstrate that to a large extent, the CeO_2 -R catalyst can tolerate water vapor, indicating that it has the potential for industrial application in desulfurization processes.

Since catalyst stability is a key factor for practical applications [62], the relevant properties of CeO_2 were examined and the results are presented in Fig. 6D. In detail, at $T = 190$ °C, the CeO_2 -R catalyst exhibits H_2S conversion of 86% and sulfur selectivity of ca. 100% in the initial 40 h, and then there is slight decrease in H_2S conversion and sulfur selectivity. As for the CeO_2 -N catalyst, initial H_2S conversion at 190 °C is only 64% with a sulphur selectivity of ca. 100%. After the initial 10 h, there is decline of H_2S conversion and sulfur selectivity. As the temperature is raised to 220 °C, H_2S conversion and sulfur selectivity over CeO_2 -R become 100% and remains so in the following 40 h, whereas in the case of CeO_2 -N, H_2S conversion (81%) and sulfur selectivity (94%) starts to decrease after 10 h and 20 h, respectively. It is speculated that the gradual decline of catalytic activities over the CeO_2 catalyst is mainly due to the deposition of produced elemental sulfur, which could occupy the active sites of catalysts. Moreover, the SEM image (Fig. S6) of the used CeO_2 -R catalyst indicates that the rod-like morphology remains. Therefore, compared with CeO_2 -N catalyst with {111} facet, the CeO_2 -R catalyst with {100} and {110} facets

displays much better durability in terms of catalytic performance.

3.3. Catalytic mechanisms

It was pointed out that the surface basic sites of catalysts play a key role in the H_2S selective oxidation [63]. H_2S adsorption on basic sites occurs prior to the oxidation reaction. We conducted CO_2 -TPD-MS investigation to assess the surface basicity of the four CeO_2 catalysts. As shown in Fig. 7A, there are CO_2 desorption at ca. 150, 300 and 520 °C, which could be ascribed, respectively, to weak CO_2 adsorption on OH groups, moderate CO_2 adsorption on metal-oxygen pairs and strong CO_2 adsorption on O^{2-} anions [64]. The amounts of surface basic sites obtained from the CO_2 -TPD-MS results are listed in Table S4. Across the four catalysts, the extents of moderate CO_2 adsorption display a decreasing order of CeO_2 -R > CeO_2 -C > CeO_2 -S > CeO_2 -N, suggesting that the amount of sites with moderate basicity is dependent on the shape of CeO_2 catalysts. As reported [65], CO_2 can interact with defect sites present on ceria surfaces to form stable carbonate species. Combined with the Raman and EPR results (Fig. 3), it is clear that the most defective CeO_2 -R catalyst has the largest amount of basic sites while the least defective CeO_2 -N catalyst has the lowest amount of basic sites for CO_2 chemisorption. In addition, the large amount of basic sites on CeO_2 -R could be partially caused by the high specific surface area of CeO_2 -R [66]. Based on the correlation between basicity and catalytic activity depicted in Fig. 7B, it is reasonable to deduce that high basicity

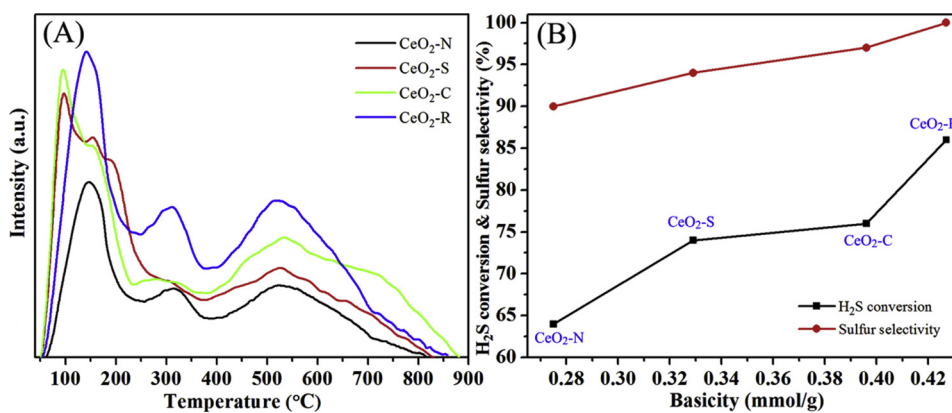


Fig. 7. (A) CO₂-TPD-MS spectra and (B) correlation between basicity and catalytic performance of CeO₂-R, CeO₂-C, CeO₂-S and CeO₂-N.

is favorable for catalytic activity. With the largest amount of basic sites, CeO₂-R shows the best catalytic performance (Fig. 5, Table 2). The above results prove that the basic properties of CeO₂ catalysts can be tailored by regulating the shape of CeO₂ nanocrystals.

Overall, CeO₂ of different shapes are distinct in concentration of oxygen vacancies, which are active sites for the adsorption of molecular oxygen. We performed O₂-TPD-MS investigation to find out the intrinsic properties of oxygen species, and the results are shown in Fig. 8A. The O₂ desorption peaks of the four catalysts could be divided into three categories: that at around 90 °C, 460 °C and 650 °C is, respectively, ascribed to the desorption of physically adsorbed O₂, chemically active surface oxygen species and lattice oxygen [67,68]. Notably, the peak intensity of chemically adsorbed oxygen over the CeO₂-R catalyst is the highest, meaning that there is enhanced chemical O₂ adsorption, which probably due to the abundant amount of vacancies on CeO₂ nanorods. Besides, the peak intensity of lattice oxygen over CeO₂-R catalyst is obviously higher, indicating that CeO₂-R has high mobility of surface lattice oxygen. Overall, the total amounts of chemically active surface oxygen and lattice oxygen species across the four catalysts show an increasing order of CeO₂-N < CeO₂-S < CeO₂-C < CeO₂-R. In consistent with the results of catalytic activity, the variation trend of H₂S conversion agrees well with that of chemically adsorbed oxygen. Meanwhile, the enrichment of active oxygen species on CeO₂-R is favorable for the oxidation reaction [69].

It is well recognized that besides surface oxygen species, the redox property of CeO₂ catalyst also influences catalytic activity. The relationship between shapes and redox properties of CeO₂ nanocrystals were evaluated by H₂-TPR. The H₂-consumption curves are presented in Fig. 8B and the amounts of H₂ consumption summarized in Table S5. There are two strong reduction peaks for the four samples: the peaks at 450–550 °C are ascribed to the reduction of capped and subsurface

oxygen species on the surface, whereas those at 700–800 °C are associated with the reduction of bulk oxygen in ceria [70]. The CeO₂-N sample exhibits two distinct reduction peaks at 530 and 770 °C, while the CeO₂-R sample shows peaks at 420 and 730 °C. The phenomena reveal that the latter is more reducible and its oxygen species are more readily available for oxidation reaction. From Table S5, it can be found that the H₂ consumption over the catalysts decrease in the sequence of CeO₂-R > CeO₂-C > CeO₂-S > CeO₂-N, which is accordance with the catalytic activity for H₂S selective oxidation. The CeO₂-R catalyst presents the highest reducibility, which may be connected with its high oxygen mobility on reactive {110} and {100} planes [71]. Referring to the results of catalytic activities, the difference in reducibility could be also explained in accordance with the formation energies of oxygen vacancies on the exposed crystal planes, which follow the order of {110} < {100} < {111} [72]. The above results suggest that the surface oxygen species and redox properties of ceria can be regulated by preparing nanocrystals with exposed planes of specific orientation.

Previous works revealed that there are various ways for H₂S adsorption on a catalyst surface [73]: (i) Reaction with –OH to form HS[–] and H₂O; (ii) Adsorption on catalyst surface, resulting in the formation of HS[–] and –OH; and (iii) Adsorption on a vacant site, followed by incorporation of S^{2–} into the catalyst lattice. To identify the adsorption pathway and reaction mechanism of H₂S on the surface of CeO₂, we performed *in situ*-DRIFTS analysis of the CeO₂-R catalyst that was H₂S-treated at different temperatures. As shown in Fig. 9, multiple bands at 1243–1482 cm^{–1} and 2578 cm^{–1} are observed after H₂S adsorption at 100 °C, which are associated with hydrogen-bonding of H₂S to the catalyst surface [74]. At 130 °C, the peak intensity of the H₂S bands decrease and new bands (1628 cm^{–1}) ascribable to the bending mode of H₂O appear, which could be related to the reaction of H₂S + [O] → S + H₂O ([O] denotes lattice oxygen) [75]. In addition, new bands at

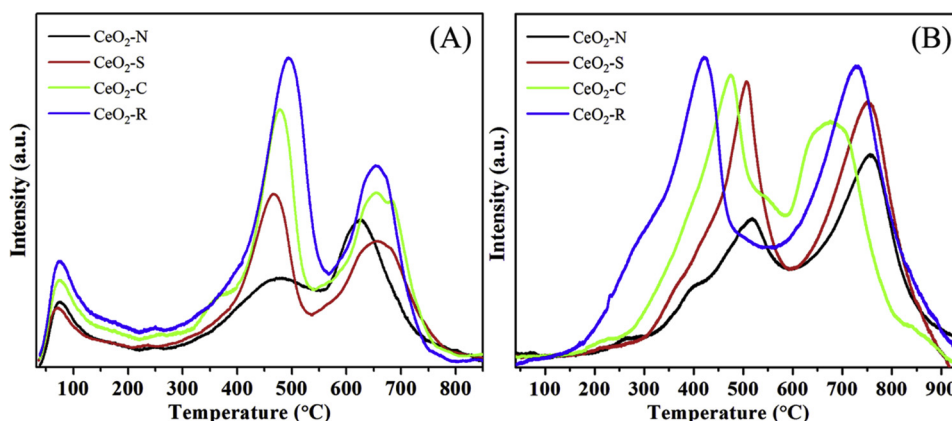


Fig. 8. (A) O₂-TPD-MS spectra and (B) H₂-TPR profiles of CeO₂-R, CeO₂-C, CeO₂-S and CeO₂-N.

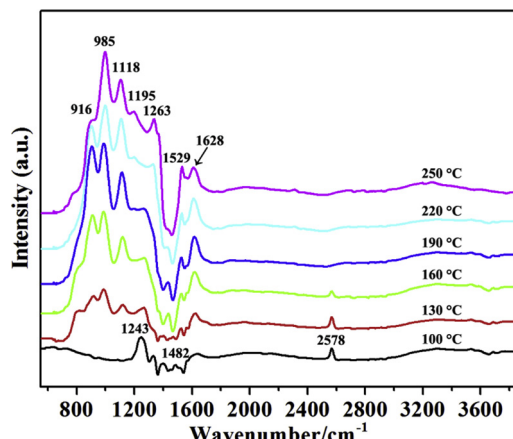


Fig. 9. DRIFTS spectra of H₂S over CeO₂-R after exposure to 5000 ppm H₂S at different temperatures.

916, 985 and 1118 cm⁻¹ assignable to sulfates are detected, suggesting the formation of sulfates. Upon reaction at 160 °C, the peak intensity of sulfates and H₂O increase and that of H₂S reduces, suggesting that the catalytic reaction is still in progress. At 220 and 250 °C, the bands of H₂S species almost disappear and new bands ascribable to surface SO₂ species at 1195 and 1263 cm⁻¹ appear in low intensity, which could be due to the oxidation of a little amount of elemental sulfur with lattice oxygen (S + 2[O] → SO₂) [76]. The results provide eloquent proof for the involvement of lattice oxygen in the H₂S selective oxidation.

It is observed that the activities of CeO₂ catalyst decreased to some extent after long-term reaction. Accordingly, XPS analysis of fresh and used CeO₂-R catalyst (after durability test) was performed. The results are presented in Fig. 10 and the relative abundances of Ce³⁺ and O_{ad} are listed in Table S1. It is found that the Ce³⁺/(Ce³⁺ + Ce⁴⁺) ratio of

used catalyst is larger than that of fresh one, which suggests the participation of Ce³⁺ and Ce⁴⁺ in H₂S oxidation. In addition, the O 1s peak intensity of lattice oxygen of used catalyst is less than that of fresh catalyst, and the O_{ad}/(O_{latt} + O_{ad}) ratio of used catalyst is bigger than that of fresh catalyst. The results confirm the participation and consumption of surface lattice oxygen in the H₂S selective oxidation reaction.

The S 2p spectra of fresh and used CeO₂-R catalyst are illustrated in Fig. 10C. There is no detection of S 2p signal over the fresh sample. As for the used CeO₂-R catalyst, there is the detection of S 2p peaks at 163.3 and 168.1 eV attributable to elemental sulfur and sulfate [77], with the former significantly higher than the latter in intensity. It is generally known that the formation of cerium sulfate would disrupt the Ce³⁺/Ce⁴⁺ redox process, resulting in retarded oxidation of Ce³⁺ to Ce⁴⁺ and causing a decrease of catalytic activity. Further characterization of the used CeO₂-R catalyst was conducted by XRD, SEM mapping and Brunauer-Emmett-Teller (BET) analyses. In the XRD spectra of used CeO₂-R, a new peak at 22.7° corresponds to elemental sulfur is observed (Fig. 10D), confirming the formation of elemental sulfur in H₂S selective oxidation [78]. The SEM mapping and EDX spectrum presented in Fig. S7 also confirm the presence of sulfur. Furthermore, the results of BET analysis show that the BET surface area (73.1 m²/g) and pore volume (0.52 cm³/g) of the used CeO₂-R are smaller than those of fresh catalyst, plausibly due to pore blockage by sulfate and element sulfur. Therefore, the decrease of catalytic activity is associated with the formation of sulfate species and condensation of sulfur in the pores of catalyst.

3.4. DFT calculations

The optimized models of an oxygen vacancy on CeO₂ {110}, {100}, and {111} surfaces are shown in Fig. 11. The formation energy of an oxygen vacancy, E_v, is estimated by the formula E_v = E_{CeO_{2-x}} + 1/2E_{O₂}

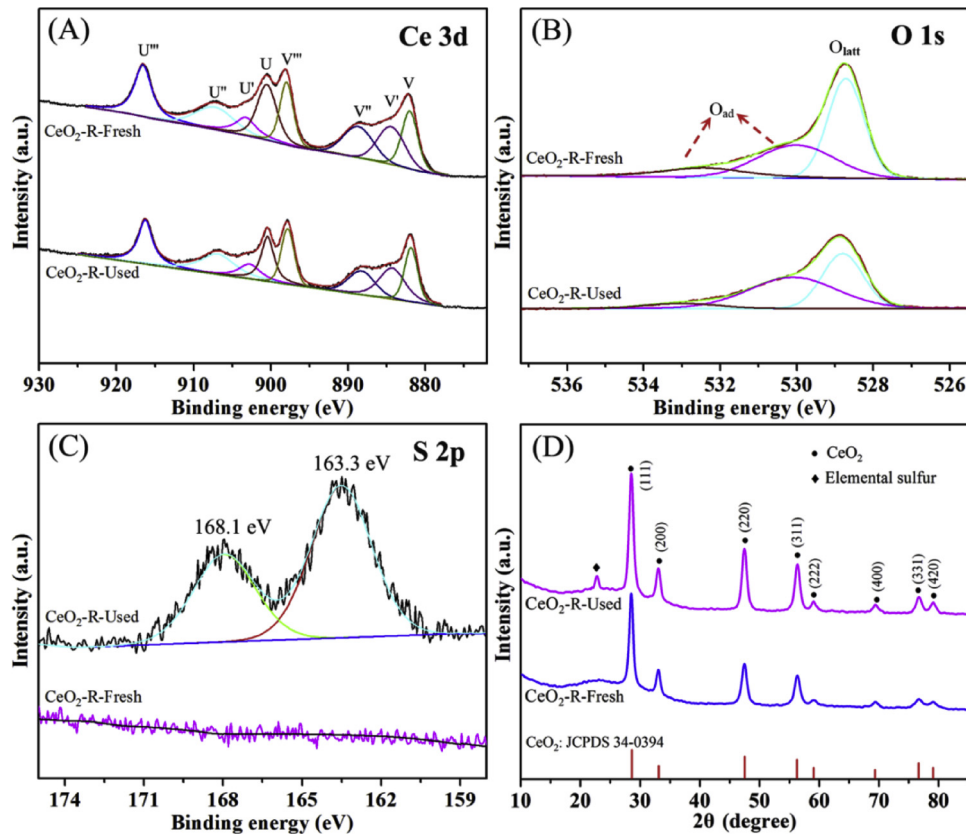


Fig. 10. (A) Ce 3d, (B) O 1s and (C) S 2p XPS spectra, and (D) XRD patterns of fresh and used CeO₂-R catalyst.

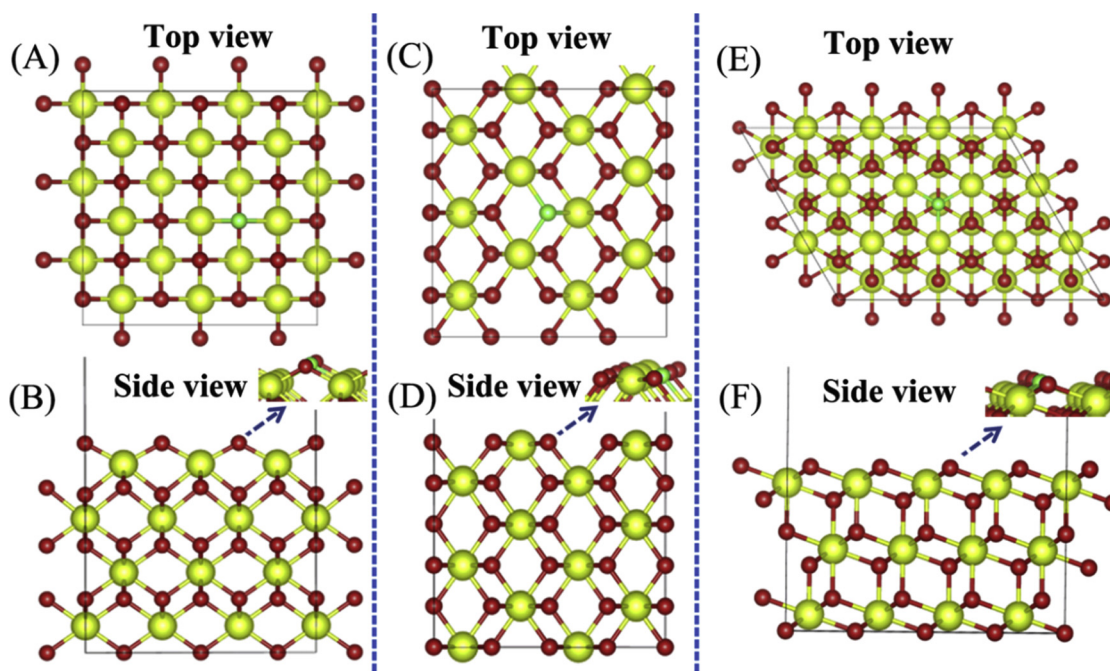


Fig. 11. (A, C, E) Top views and (B, D, F) side views of the optimal geometries of oxygen vacancies: (A, B) CeO_2 {100}, (C, D) CeO_2 {110}, and (E, F) CeO_2 {111} surfaces (yellow, Ce; red, O; green, O atoms) (For interpretation of the references to colour in this figure legend, the reader is referred to the web version of this article).

$-E_{\text{CeO}_2}$, where E_{CeO_2-x} represents the energy of a reduced CeO_2 surface containing an oxygen vacancy. E_{CeO_2} and E_{O_2} are the energy of optimal stoichiometric CeO_2 surface and an O_2 molecule [79,80]. The calculated E_v values over the CeO_2 surfaces rank in the order of: {110} (1.85 eV) < {100} (1.94 eV) < {111} (2.57 eV). The results suggest that the formation of oxygen vacancy occurs more readily on CeO_2 {110} and {100} planes, in accordance with the experimental results and previous DFT work [81]. The structure of O_2 adsorbed on an oxygen vacancy of reduced CeO_2 {110} surface is shown in Fig. S8. The adsorption energy (E_{adsorb} , $E_{\text{adsorb}} = E_{\text{Ov-O}_2} - E_{\text{Ov}} - E_{\text{O}_2}$) of O_2 on the oxygen vacancy is predicted to be -1.74 eV, indicating that the adsorption process is strongly exothermic, which is thermodynamically advantageous [82]. Moreover, after adsorption the O–O bond distance is 1.437 Å, larger than that of a free O_2 molecule (1.233 Å). Therefore, oxygen molecule is easily activated by the defect CeO_2 surface.

The above results demonstrate that the CeO_2 -R catalyst with well-defined {100} and {110} planes possesses large amounts of oxygen vacancies. Since the dissociation of H_2S is an essential step in H_2S selective oxidation, we studied the dissociation of H_2S and SH , as well as the desorption of final S product over the reduced CeO_2 {110} surface. As for H_2S adsorption, five configurations with different orientations of H_2S were investigated, as depicted in Fig. S9. Our results indicate that the most stable model for H_2S adsorption is that on the surface of V- H_2S (c), in which the H_2S molecule is situated at the oxygen vacancy with an adsorption energy of -0.63 eV, implying that the oxygen vacancy is in favor of H_2S adsorption [83]. After adsorption, The S–H bond lengths are 1.362 and 1.346 Å, the former is bigger than that of a H_2S molecule (1.348 Å), suggesting that one of the S–H bonds was broken during the adsorption process [84]. In the case of SH adsorption modes shown in Table S6, V-SH(d) is the most stable model. In this structure, the S atom is at a Ce^{3+} site while the hydrogen atom interacts with a neighboring O through hydrogen bonding. The S–Ce bond length is 2.996 Å, and the dissociated H is adsorbed on an O site connected with Ce^{3+} . The S–H bond length is 1.361 Å, bigger than that of a free H_2S molecule (1.348 Å), suggesting that the S–H bond was broken during SH adsorption. The results indicate that SH is further dissociated on the reduced CeO_2 {110} surface [85]. Besides, the H atom originated from SH is connected to an oxygen atom of surface ceria, forming O–H bond of

0.993 Å in length, a value close to the that (0.958 Å) of a free H_2O molecule. Bader charge analysis [86] suggests that the surface OH has got 0.8e electrons, which is close to the charge of hydroxyl ($-\text{OH}$), and the formed OH might continue to form a water molecule through interaction with another surface H atom. The generation of H_2O has been detected in the characterization of H_2S oxidation based on *in situ*-DRIFTS technique.

Accordingly, the dissociation of H_2S on the reduced {110} surface of ceria can be illustrated as depicted in Fig. 12. The most stable adsorption structure of H_2S is selected as the initial state, and with an energy of -1.55 eV, the first dissociation process (step 1, $\text{H}_2\text{S} \rightarrow \text{SH} + \text{H}$) is facile. In the second dissociation process (step 2, $\text{SH} \rightarrow \text{S} + \text{H}$), despite the lower dissociation energy (-0.07 eV), the negative energy is still beneficial for dissociation, especially at high temperatures.

It should be noted that the process of H_2S oxidation involves sulfur desorption from the ceria surface. The computation process of sulfur desorption from a reduced CeO_2 {110} surface is presented in Table S7. The energy for S desorption can be calculated by the formula: $\Delta E = E_{\text{Ov-2H}} + E\left(\frac{\text{S}}{8}\right) - E_{\text{Ov-S-2H}}$. The ΔE value is 0.25 eV and the S–Ce bond length is 2.580 Å. The low desorption energy of S indicates that it is

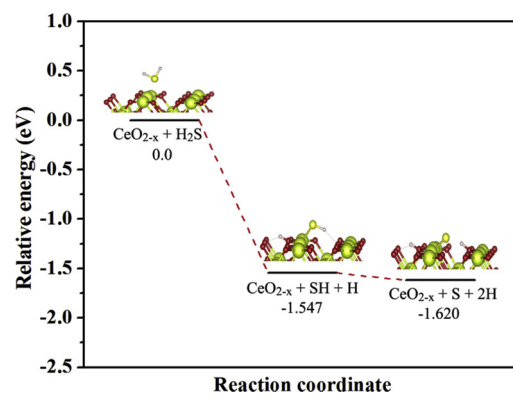


Fig. 12. Variations of the relative energies of H_2S dissociation on reduced CeO_2 {110} surface.

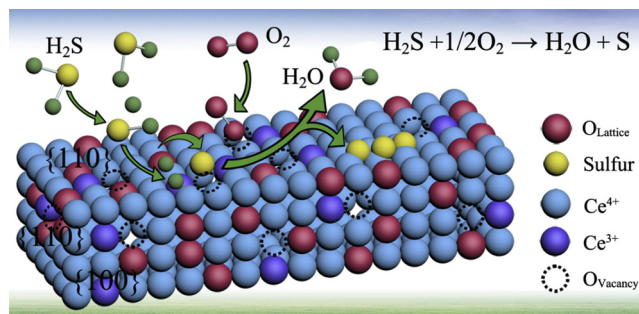


Fig. 13. Schematic of H_2S oxidation over the $\text{CeO}_2\text{-R}$ catalyst.

easy to have S desorbed from the reduced $\text{CeO}_2\{110\}$ surface.

On the basis of the above results, we offered a possible reaction mechanism for selective oxidation of H_2S over the $\text{CeO}_2\text{-R}$ catalyst which is endowed with well-defined $\{110\}$ and $\{100\}$ crystal planes (Fig. 13). The H_2S molecules first diffuse into the pores and adsorb on surface basic sites and oxygen vacancies. Then the adsorbed H_2S species dissociate to HS^- or S^{2-} ions. Subsequently the HS^- ions are oxidized to elemental sulfur by surface active oxygen and/or lattice oxygen species of reduced CeO_2 , together with the reduction of Ce^{4+} and the formation of oxygen vacancies [87]. Then, the active oxygen species are replenished through the adsorption of gaseous O_2 , leading to the oxidation of Ce^{3+} to Ce^{4+} . Overall, the outstanding catalytic activities and durability of $\text{CeO}_2\text{-R}$ catalyst would be related to the porous structure, abundant oxygen vacancies and moderate basic properties on the surface of the catalyst.

4. Conclusions

The shape dependence of H_2S selective oxidation over ceria nanocrystals (rods, cubes, spheres, and nanoparticles) was investigated in detail. The structure-property relationships established in the present research indicate that the oxygen vacancy on the CeO_2 surface is the active site for H_2S conversion. With well-defined $\{100\}$ and $\{110\}$ planes, the CeO_2 catalyst of rod-like morphology possesses high concentration of oxygen vacancies (confirmed by Raman, EPR and XPS) that benefits the conversion of lattice oxygen to active oxygen, consequently results in promoted reactivity for H_2S selective oxidation. In addition, the $\text{CO}_2\text{-TPD-MS}$ results show that the $\text{CeO}_2\text{-R}$ catalyst with enhanced surface basicity facilitates adsorption and dissociation of H_2S , ultimately leading to high catalytic performance. Moreover, the presence of hierarchically porous structure enables high catalyst stability and sulfur selectivity by restricting sulfate formation and S condensation. The results of DFT calculations indicate that H_2S molecule dissociates readily on the reduced $\text{CeO}_2\{110\}$ surface, consistent with our experimental results. The findings of the present work give new insights into the optimization of CeO_2 -based catalysts for H_2S selective oxidation.

Acknowledgements

This work was financially supported by the National Science Fund for Distinguished Young Scholars of China (21825801), National Natural Science Foundation of China (21603034, 21773030), National Key Research and Development Program of China (2018YFA0209304) and the Natural Science Foundation of Fujian Province (2017J05022).

Appendix A. Supplementary data

Supplementary material related to this article can be found, in the online version, at doi:<https://doi.org/10.1016/j.apcatb.2019.04.014>.

References

- [1] M.S. Shah, M. Tsapatsis, J.I. Siepmann, Chem. Rev. 117 (2017) 9755–9803.
- [2] M. Flytzani-Stephanopoulos, M. Sakbodin, Z. Wang, Science 312 (2006) 1508–1510.
- [3] F. Kamali, M.M. Eskandari, A. Rashidi, M. Baghalha, M. Hassanasi, T. Hamzehlouyan, J. Hazard. Mater. 364 (2019) 218–226.
- [4] M. Dan, S. Wei, D.E. Doronkin, Y. Li, Z. Zhao, S. Yu, J.-D. Grunwaldt, Y. Lin, Y. Zhou, Appl. Catal. B-Environ. 243 (2019) 790–800.
- [5] X. Zong, J. Han, B. Seger, H. Chen, G. Lu, C. Li, L. Wang, Angew. Chem. Int. Ed. 53 (2014) 4399–4403.
- [6] M. Dan, A. Prakash, Q. Cai, J. Xiang, Y. Ye, Y. Li, S. Yu, Y. Lin, Y. Zhou, Solar RRL 3 (2019) 1800237.
- [7] L. Shen, G. Lei, Y. Fang, Y. Cao, X. Wang, L. Jiang, Chem. Commun. 54 (2018) 2475–2478.
- [8] K.V. Bineesh, D.-K. Kim, D.-W. Kim, H.-J. Cho, D.-W. Park, Energ. Environ. Sci. 3 (2010) 302–310.
- [9] X. Zhang, Z. Wang, Y. Tang, N. Qiao, Y. Li, S. Qu, Z. Hao, Catal. Sci. Technol. 5 (2015) 4991–4999.
- [10] H.M. Tasdemir, S. Yasyerli, N. Yasyerli, Int. J. Hydrog. Energy 40 (2015) 9989–10001.
- [11] J. Jones, H. Xiong, A.T. Delariva, E.J. Peterson, H. Pham, S.R. Challa, G. Qi, S. Oh, M.H. Wiebenga, P.H.N. Xi, Science 353 (2016) 150–154.
- [12] G.N. Vayssilov, Y. Lykhach, A. Migani, T. Staudt, G.P. Petrova, N. Tsud, T. Skala, A. Bruix, F. Illas, K.C. Prince, V. Matolin, K.M. Neyman, J. Libuda, Nat. Mater. 10 (2011) 310–315.
- [13] W. Si, Y. Wang, Y. Peng, J. Li, Angew. Chem. Int. Ed. 54 (2015) 7954–7957.
- [14] Y.Q. Su, I.A.W. Filot, J.X. Liu, E.J.M. Hensen, ACS Catal. 8 (2018) 75–80.
- [15] F. Zhang, X. Zhang, Z. Hao, G. Jiang, H. Yang, S. Qu, J. Hazard. Mater. 342 (2018) 749–757.
- [16] V. Palma, D. Barba, Fuel 135 (2014) 99–104.
- [17] S. Yasyerli, G. Dogu, T. Dogu, Catal. Today 117 (2006) 271–278.
- [18] S. Zhang, Z.Q. Huang, Y. Ma, W. Gao, J. Li, F. Cao, L. Li, C.R. Chang, Y. Qu, Nat. Commun. 8 (2017) 15266.
- [19] X. Zhang, P. Tian, W. Tu, Z. Zhang, J. Xu, Y.F. Han, ACS Catal. 8 (2018) 5261–5275.
- [20] Y. Xie, J. Wu, G. Jing, H. Zhang, S. Zeng, X. Tian, X. Zou, J. Wen, H. Su, C.-J. Zhong, Appl. Catal. B Environ. 239 (2018) 665–676.
- [21] S. Wang, L. Zhao, W. Wang, Y. Zhao, G. Zhang, X. Ma, J. Gong, Nanoscale 5 (2013) 5582–5588.
- [22] C.M. Parlett, K. Wilson, A.F. Lee, Chem. Soc. Rev. 42 (2013) 3876–3893.
- [23] M. Chen, Y. Zhang, L. Xing, Y. Liao, Y. Qiu, S. Yang, W. Li, Adv. Mater. 29 (2017) 1–28.
- [24] C. Sun, H. Li, L. Chen, Energy Environ. Sci. 5 (2012) 8475–8505.
- [25] S. Agarwal, L. Lefferts, B.L. Mojat, D.M. Ligthart, E.J. Hensen, D.R. Mitchell, W.J. Erasmus, B.G. Anderson, E.J. Olivier, J.H. Neethling, ChemSusChem 6 (2013) 1898–1906.
- [26] G. Kresse, J. Furthmüller, Comp. Mater. Sci. 6 (1996) 15–50.
- [27] G. Kresse, J. Furthmüller, Phys. Rev. B 54 (1996) 11169–11186.
- [28] J.P. Perdew, K. Burke, M. Ernzerhof, Phys. Rev. Lett. 77 (1996) 3865–3868.
- [29] S. Fabris, G. Vicario, G. Balducci, S. de Gironcoli, S. Baroni, J. Phys. Chem. B 109 (2005) 22860–22867.
- [30] G. Spezzati, A.D. Benavidez, A.T. DeLaRiva, Y. Su, J.P. Hofmann, S. Asahina, E.J. Olivier, J.H. Neethling, J.T. Miller, A.K. Datye, Appl. Catal. B Environ. 243 (2019) 36–46.
- [31] H. Huang, Q. Dai, X. Wang, Appl. Catal. B Environ. 158–159 (2014) 96–105.
- [32] Z. Ma, S. Zhao, X. Pei, X. Xiong, B. Hu, Catal. Sci. Technol. 7 (2017) 191–199.
- [33] C. Li, Y. Sun, I. Djerdj, P. Voepel, C.-C. Sack, T. Weller, Rd. Ellinghaus, J. Sann, Y. Guo, B.C. Smarsly, ACS Catal. 7 (2017) 6453–6463.
- [34] L. Qi, Q. Yu, Y. Dai, C. Tang, L. Liu, H. Zhang, F. Gao, L. Dong, Y. Chen, Appl. Catal. B Environ. 119–120 (2012) 308–320.
- [35] S.C. Rood, H.B. Ahmet, A. Gomez-Ramon, L. Torrente-Murciano, T.R. Reina, S. Eslava, Appl. Catal. B Environ. 242 (2019) 358–368.
- [36] B. Liu, C. Li, G. Zhang, X. Yao, S.S. Chuang, Z. Li, ACS Catal. 8 (2018) 10446–10456.
- [37] L. Nie, D. Mei, H. Xiong, B. Peng, Z. Ren, X.I.P. Hernandez, A. DeLaRiva, M. Wang, M.H. Engelhard, L. Kovarik, Science 358 (2017) 1419–1423.
- [38] Q. Xie, H. Zhang, J. Kang, J. Cheng, Q. Zhang, Y. Wang, ACS Catal. 8 (2018) 4902–4916.
- [39] P. Sudarsanam, B. Hillary, B. Mallesham, B.G. Rao, M.H. Amin, A. Nafady, A.M. Alsalme, B.M. Reddy, S.K. Bhargava, Langmuir 32 (2016) 2208–2215.
- [40] Y. Li, Z. Wei, F. Gao, L. Kovarik, R.A.L. Baylon, C.H.F. Peden, Y. Wang, ACS Catal. 5 (2015) 3006–3012.
- [41] W. Yang, C. Li, H. Wang, X. Li, W. Zhang, H. Li, Appl. Catal. B Environ. 239 (2018) 233–244.
- [42] Y. Cao, L. Zhao, T. Gutmann, Y. Xu, L. Dong, G. Buntkowsky, F. Gao, J. Phys. Chem. C 122 (2018) 20402–20409.
- [43] J. Mei, Y. Ke, Z. Yu, X. Hu, Z. Qu, N. Yan, Chem. Eng. J. 320 (2017) 124–134.
- [44] J.A. Farmer, C.T. Campbell, Science 329 (2010) 933–936.
- [45] Z. Hu, X. Liu, D. Meng, Y. Guo, Y. Guo, G. Lu, ACS Catal. 6 (2016) 2265–2279.
- [46] W.W. Wang, W.Z. Yu, P.P. Du, H. Xu, Z. Jin, R. Si, C. Ma, S. Shi, C.J. Jia, C.H. Yan, ACS Catal. 7 (2017) 1313–1329.
- [47] W. Zhao, X. Zheng, S. Liang, X. Zheng, L. Shen, F. Liu, Y. Cao, Z. Wei, L. Jiang, Green Chem. 20 (2018) 4645–4654.
- [48] C. Yang, X. Yu, S. Heissler, P.G. Weidler, A. Nefedov, Y. Wang, C. Woll, T. Kropp, J. Paier, J. Sauer, Angew. Chem. Int. Ed. 56 (2017) 16399–16404.
- [49] X. Zheng, X. Chen, J. Chen, Y. Zheng, L. Jiang, Chem. Eng. J. 297 (2016) 148–157.

- [50] Y. Xiao, X. Zheng, X. Chen, L. Jiang, Y. Zheng, Ind. Eng. Chem. Res. 56 (2017) 1687–1695.
- [51] J. Wang, Q. Ma, Y. Wang, Z. Li, Z. Li, Q. Yuan, Chem. Soc. Rev. 47 (2018) 8766–8803.
- [52] M.Y. Shin, M.N. Chang, D.W. Park, J.S. Chung, Appl. Catal. A Gen. 211 (2001) 213–225.
- [53] E. Ghasemiy, H.B. Motejadded, A. Rashidi, T. Hamzehlouyan, Z. Yousefian, T. Taiwan Inst. Chem. E. 85 (2018) 121–131.
- [54] X.X. Zheng, L.J. Shen, X.P. Chen, X.H. Zheng, C.T. Au, L.L. Jiang, Inorg. Chem. 57 (2018) 10081–10089.
- [55] M. Cargnello, V.V. Doan-Nguyen, T.R. Gordon, R.E. Diaz, E.A. Stach, R.J. Gorte, P. Fornasiero, C.B. Murray, Science 341 (2013) 771–773.
- [56] X. Chen, Y. Zheng, F. Huang, Y. Xiao, G. Cai, Y. Zhang, Y. Zheng, L. Jiang, ACS Catal. 8 (2018) 11016–11028.
- [57] N.M. Schweitzer, J.A. Schaidle, O.K. Ezekeye, X. Pan, S. Linic, L.T. Thompson, J. Am. Chem. Soc. 133 (2011) 2378–2381.
- [58] X. Zhang, Y. Tang, N. Qiao, Y. Li, S. Qu, Z. Hao, Appl. Catal. B Environ. 176 (2015) 130–138.
- [59] X. Zhang, G. Dou, Z. Wang, J. Cheng, H. Wang, C. Ma, Z. Hao, Catal. Sci. Technol. 3 (2013) 2778–2785.
- [60] K.V. Bineesh, D.-K. Kim, M.-I. Kim, M. Selvaraj, D.-W. Park, Dalton Trans. 40 (2011) 3938–3945.
- [61] F. Hu, J. Chen, Y. Peng, H. Song, K. Li, J. Li, Chem. Eng. J. 331 (2018) 425–434.
- [62] H. Zhao, H. Song, L. Chou, J. Zhao, J. Yang, L. Yan, Catal. Sci. Technol. 7 (2017) 3258–3267.
- [63] F. Zhang, X. Zhang, G. Jiang, N. Li, Z. Hao, S. Qu, Chem. Eng. J. 348 (2018) 831–839.
- [64] L. He, B. Liang, L. Li, X. Yang, Y. Huang, A. Wang, X. Wang, T. Zhang, ACS Catal. 5 (2015) 1623–1628.
- [65] Z. Wu, A.K. Mann, M. Li, S.H. Overbury, J. Phys. Chem. C 119 (2015) 7340–7350.
- [66] D. Wang, X. Zhang, J. Ma, H. Yu, J. Shen, W. Wei, Catal. Sci. Technol. 6 (2016) 1530–1545.
- [67] F. Esch, S. Fabris, L. Zhou, T. Montini, C. Africh, P. Fornasiero, G. Comelli, R. Rosei, Science 309 (2005) 752–755.
- [68] M. Sathiya, G. Rousse, K. Ramesha, C.P. Laissa, H. Vezin, M.T. Sougrati, M.L. Doublet, D. Foix, D. Gonbeau, W. Walker, A.S. Prakash, M. Ben Hassine, L. Dupont, J.M. Tarascon, Nat. Mater. 12 (2013) 827–835.
- [69] S. Yang, W. Zhu, Z. Jiang, Z. Chen, J. Wang, Appl. Surf. Sci. 252 (2006) 8499–8505.
- [70] Y. Zheng, K. Li, H. Wang, Y. Wang, D. Tian, Y. Wei, X. Zhu, C. Zeng, Y. Luo, J. Catal. 344 (2016) 365–377.
- [71] X. Liu, K. Zhou, L. Wang, B. Wang, Y. Li, J. Am. Chem. Soc. 131 (2009) 3140–3141.
- [72] Q. Dai, S. Bai, Z. Wang, X. Wang, G. Lu, Appl. Catal. B Environ. 126 (2012) 64–75.
- [73] X. Zhang, Z. Wang, N. Qiao, S. Qu, Z. Hao, ACS Catal. 4 (2014) 1500–1510.
- [74] C.L. Liu, T.T. Chuang, I.G.D. Lana, J. Catal. 26 (1972) 474–476.
- [75] L. Shen, X. Zheng, G. Lei, X. Li, Y. Cao, L. Jiang, Chem. Eng. J. 346 (2018) 238–248.
- [76] A.M. Deane, D.L. Griffiths, I.A. Lewis, J.A. Winter, A.J. Tench, J. Chem. Soc. Faraday Trans. 71 (1975) 1005–1012.
- [77] M.D. Soriano, J. Jiménez-Jiménez, P. Concepción, A. Jiménez-López, E. Rodríguez-Castellón, J.M.L. Nieto, Appl. Catal. B Environ. 92 (2009) 271–279.
- [78] F. Sun, J. Liu, H. Chen, Z. Zhang, W. Qiao, D. Long, L. Ling, ACS Catal. 3 (2013) 862–870.
- [79] A.D. Mayernick, M.J. Janik, J. Phys. Chem. C 112 (2008) 14955–14964.
- [80] Z. Wu, M. Li, S.H. Overbury, J. Catal. 285 (2012) 61–73.
- [81] Z. Wu, M. Li, D.R. Mullins, S.H. Overbury, ACS Catal. 2 (2012) 2224–2234.
- [82] B.-T. Teng, S.-Y. Jiang, Z.-X. Yang, M.-F. Luo, Y.-Z. Lan, Surf. Sci. 604 (2010) 68–78.
- [83] S. Zhao, L. Ling, B. Wang, R. Zhang, D. Li, Q. Wang, J. Wang, J. Phys. Chem. C 119 (2015) 7678–7688.
- [84] S. Li, Z. Lu, Z. Yang, X. Chu, Y. Zhang, D. Ma, Int. J. Hydrogen. Energy 39 (2014) 1957–1966.
- [85] D. Marrocchelli, B. Yildiz, J. Phys. Chem. A 116 (2012) 2411–2424.
- [86] G. Henkelman, A. Arnaldsson, H. Jónsson, Comp. Mater. Sci. 36 (2006) 354–360.
- [87] A. Trovarelli, J. Llorca, ACS Catal. 7 (2017) 4716–4735.